AGU PUBLICATIONS

Geophysical Research Letters

RESEARCH LETTER
10.1002/2015GL065806

Key Points:
- We find heterogeneous melt across the submarine terminus of a Greenland outlet glacier
- Discharge through small subglacial outlets can drive large melt rates
- Terminus undercutting increases calving and may alter plume dynamics

Supporting Information:
- Text S1 and Figures S1–S3
- Movie S1
- Movie S2
- Movie S3
- Movie S4

Correspondence to:
M. J. Fried,
mfried@ig.utexas.edu

Citation:
Fried, M. J., G. A. Catania, T. C. Bartholomaus, D. Duncan, M. Davis, L. A. Stearns, J. Nash, E. Shroyer, and D. Sutherland (2015), Distributed subglacial discharge drives significant submarine melt at a Greenland tidewater glacier, *Geophys. Res. Lett.*, *42*, 9328–9336, doi:10.1002/2015GL065806.

Received 17 AUG 2015
Accepted 21 OCT 2015
Accepted article online 26 OCT 2015
Published online 11 NOV 2015

©2015. American Geophysical Union. All Rights Reserved.

Distributed subglacial discharge drives significant submarine melt at a Greenland tidewater glacier

M. J. Fried[1,2], G. A. Catania[1,2], T. C. Bartholomaus[1], D. Duncan[1], M. Davis[1], L. A. Stearns[3], J. Nash[4], E. Shroyer[4], and D. Sutherland[5]

[1]Institute for Geophysics, University of Texas at Austin, Austin, Texas, USA, [2]Department of Geology, University of Texas at Austin, Austin, Texas, USA, [3]Department of Geology, University of Kansas, Lawrence, Kansas, USA, [4]College of Earth, Ocean, and Atmospheric Sciences, Oregon State University, Corvalis, Oregon, USA, [5]Department of Geological Sciences, University of Oregon, Eugene, Oregon, USA

Abstract Submarine melt can account for substantial mass loss at tidewater glacier termini. However, the processes controlling submarine melt are poorly understood due to limited observations of submarine termini. Here at a tidewater glacier in central West Greenland, we identify subglacial discharge outlets and infer submarine melt across the terminus using direct observations of the submarine terminus face. We find extensive melting associated with small discharge outlets. While the majority of discharge is routed to a single, large channel, outlets not fed by large tributaries drive submarine melt rates in excess of 3.0 m d^{-1} and account for 85% of total estimated melt across the terminus. Nearly the entire terminus is undercut, which may intersect surface crevasses and promote calving. Severe undercutting constricts buoyant outflow plumes and may amplify melt. The observed morphology and melt distribution motivate more realistic treatments of terminus shape and subglacial discharge in submarine melt models.

1. Introduction

The Greenland Ice Sheet lost mass at an increasing rate during the last decade, in part due to the increase in ice loss from the fronts of large marine-terminating outlet glaciers [*van den Broeke et al.*, 2009; *Rignot et al.*, 2011; *Shepherd et al.*, 2012; *Enderlin et al.*, 2014]. A change in the ocean's forcing at the ice/ocean boundary is a leading hypothesis to explain these increased mass losses [*Murray et al.*, 2010; *Rignot et al.*, 2010; *Straneo et al.*, 2011]. At the terminus, subglacial discharge plays an important role in controlling ice loss to the ocean by driving submarine melt and promoting calving [*O'Leary and Christoffersen*, 2013; *Straneo et al.*, 2011; *Bartholomaus et al.*, 2013; *Motyka et al.*, 2013; *Inall et al.*, 2014; *Rignot et al.*, 2015]. These processes can result in rapid outlet glacier dynamic changes through reduction of along-flow gradients in resistive stresses, affecting fast ice flow and, in turn, terminus retreat [*Nick et al.*, 2009; *Seale et al.*, 2011].

Despite its importance, several factors limit our understanding of how subglacial discharge influences submarine melt and calving. First, thick glacier ice and iceberg-choked fjords generally obscure meltwater routing to and discharge across the terminus. While it is hypothesized that the discharge of subglacial water into the proglacial fjord at discrete points influences submarine melt rates [*Jenkins*, 2011; *Slater et al.*, 2015; *Straneo and Cenedese*, 2015], few observations of the size, number, and locations of channels exist. The extent to which more abundant, secondary channel outlets influence melt at the terminus remains unexplored despite the large rates of submarine melt they can potentially drive [*Slater et al.*, 2015]. Second, the morphology of the submarine terminus face is largely unknown (with the exception of *Rignot et al.* [2015]). The shape of the terminus face may affect the formation of buoyant melt plumes, their ability to melt the glacier front, and calving [*Jenkins*, 2011; *Xu et al.*, 2012, 2013; *Kimura et al.*, 2014]. Finally, previous submarine melt rate estimates—those derived from both heat and salt budgets [*Rignot et al.*, 2010; *Motyka et al.*, 2013] and mass continuity [*Motyka et al.*, 2011]—are unable to elucidate how the magnitude of submarine melt varies spatially across the terminus and in relation to the location of subglacial channels. In this paper, we work to resolve these issues and identify the impact that distributed subglacial discharge has on submarine melt.

We pair observations from multibeam bathymetry and satellite imagery with a predictive model of subglacial water routing to identify subglacial discharge outlets and their influence on the morphology of the terminus face at Kangerlussuup Sermia (KS), a tidewater glacier in central West Greenland (71°27′N, 51°20′W; Figure 1). We then use the observed terminus face morphology to estimate submarine melt rates at each point along

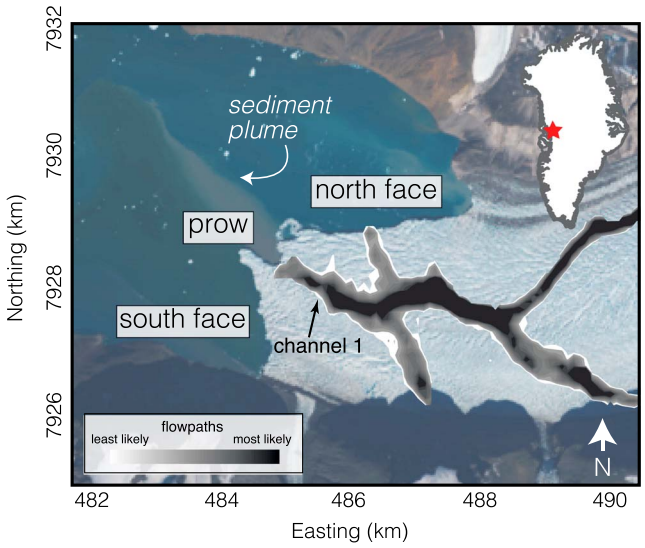


Figure 1. KS study area. Landsat 8 image (14 July 2014) showing the KS terminus region. Modeled subglacial water flow path likelihoods are shown in gray scale.

the glacier terminus. Finally, we provide further support for a mechanism by which observed melt-driven undercutting facilitates calving via connections to closely spaced surface crevasses [*Motyka et al.*, 2003].

2. Data and Methods

2.1. Multibeam Bathymetry

To investigate how subglacial discharge affects the shape of the glacier terminus, we surveyed the submarine portion of the KS terminus using a multibeam sonar system (Figure 2). Multibeam bathymetry data were collected on 21 and 23 July 2013 using a pole-mounted RESON SeaBat 7111 Multibeam Sonar System. Positioning data were acquired using an Applanix POS/MV model 320 positioning and orientation system. The survey operated at 100 kHz with 301 equi-angle beams, and we constrained the sound velocity profile at the time of the survey using in situ conductivity-temperature-depth casts. We collected data along the submarine calving face by inserting a 15° wedge into the multibeam sonar system mount to maximize vertical imaging. The resulting point cloud data represent individual measurements of the terminus location and were processed using Caris software to remove anomalous pings and to merge multibeam returns with positioning and orientation data.

In order to quantify the shape of the submarine terminus face across the entire width of the glacier, we extracted 193 terminus cross sections (spaced every ~27 m) through the multibeam point cloud, each oriented locally normal to the terminus face. For each cross section we identified the seafloor depth, d, at the grounding line and the height, h, of the seaward most point on the terminus face above the seafloor (Figure 3b). We also define the undercut length, l, as the horizontal distance between the seaward most point and the grounding line at each cross section (Figure 3b).

2.2. Submarine Melt Estimates

We estimate the submarine melt rate by assuming that any overhang of the submarine glacier terminus is due to melt, since calving from the bottom of the terminus is unlikely to occur without disrupting the ice above it and internal ice deformation is minimal compared to sliding for fast flowing, thin, gently sloping glaciers [*Cuffey and Paterson*, 2010]. These assumptions are supported both by the smooth appearance of imaged overhangs (mass lost due to calving would likely produce corners and sharp edges) and the prevalence of subvertical surface crevasses throughout the terminus region (calving is most likely to occur along these preexisting crevasses, and not at the ~45° angles commonly found for overhang roofs). Thus, we use the size of the overhang cavity to estimate the depth-averaged submarine melt rate. We assume that the midsummer face we imaged was in dynamic equilibrium; that is, while individual cross sections may change shape due to stochastic calving events, the overall amount of undercutting, averaged over the entire width of terminus, is steady. Satellite observations of glacier speed and terminus position (Figure 3a) and RACMO2.3 runoff estimates (*Ettema et al.*, 2009) immediately prior to and during our survey do not suggest any significant changes in glacier dynamics that might violate this assumption. Thus, the terminus face within the overhang (over height h) melts at the rate $\dot{m}_h = \vec{u} \cdot \hat{n} - dL/dt$, where $\vec{u} \cdot \hat{n}$ is the ice velocity normal to the terminus and dL/dt is the rate of change of the glacier terminus position. Following convention, $\dot{m}_h$ is defined positive up-glacier, whereas $\vec{u} \cdot \hat{n}$ and dL/dt are positive toward the fjord. We obtain ice velocities from 16 July to 27 July 2013 TerraSAR-X data [*Joughin et al.*, 2014] and use the associated TerraSAR-X imagery to identify dL/dt during the time of our multibeam survey. While the overall terminus position did not change significantly over the observation period, large dL/dt values caused by localized calving events represent a source

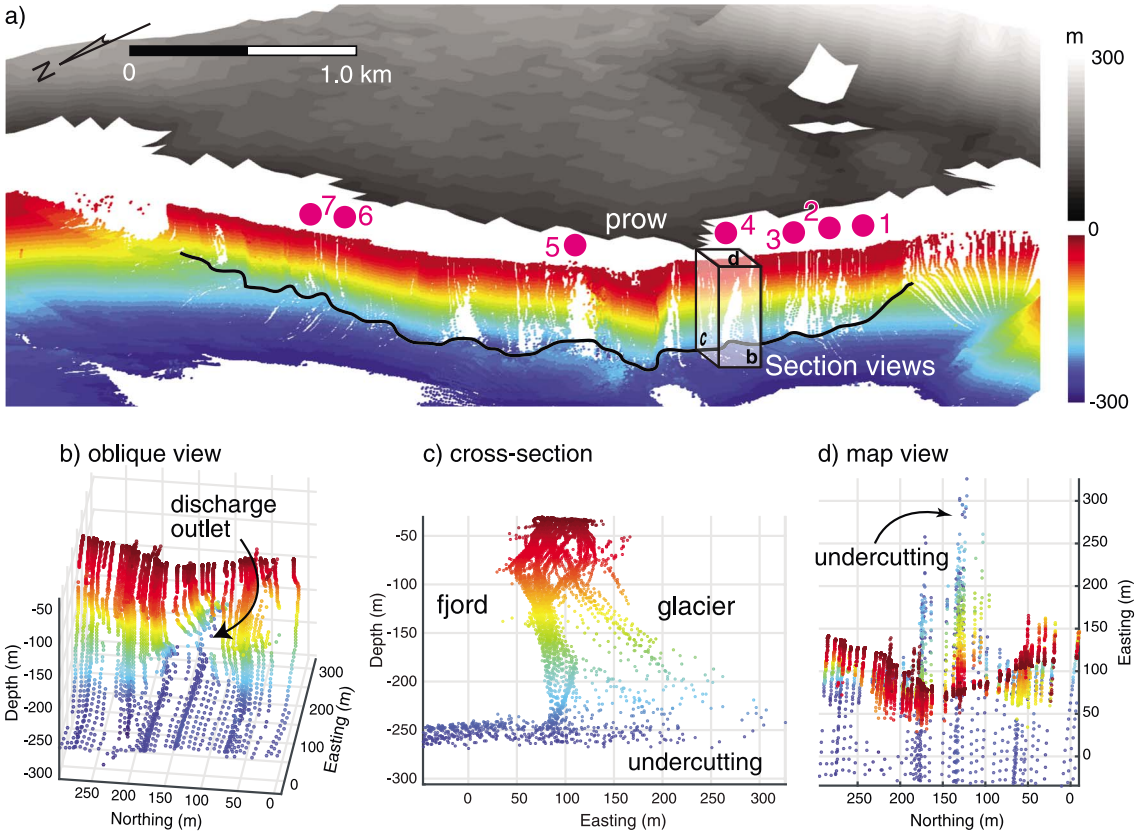


Figure 2. Perspective view of the KS ice/ocean interface and near-terminus hydrology. Glacier terminus shown with GIMP topography (gray scale) and multibeam bathymetry (jet color scale). Grounding line identified from multibeam bathymetry is shown in black. Pink dots 1–7 refer to identified subglacial discharge outlet locations. (b–d) Section views show close-ups of the multibeam point cloud illuminating localized undercutting at discharge outlet #4 from three different angles.

of local noise that obscures the patterns we seek to reveal. Thus, we calculate the mean dL/dt (0.30 m d^{-1}) from the distribution of observed length changes and use this value at each cross section in our melt estimates. The depth-averaged melt rate at a given cross section through the submarine terminus is thus $\dot{m} = h(\vec{u} \cdot \hat{n} - dL/dt)/d$. Our calculation does not consider ice loss above the seaward most point, which may occur through either melt or calving; in this regard, our melt rates are conservative. The flux of ice lost due to submarine melt, Q_i, is calculated as, $Q_i = \overline{m} A_w$, where $\overline{m}$ is the terminus-averaged submarine melt rate and A_w is the vertical, submerged terminus area.

Uncertainty in our calculation of the depth-averaged submarine melt rate is related to the uncertainties in both the ice velocity and multibeam data sets and our consideration of dL/dt. Measured ice velocities have a mean error of 0.08 m d^{-1} [*Joughin et al.*, 2014]. The multibeam point cloud is accurate to within 3–5 m horizontally and 15–25 cm radially from the ship, as reported by the POS/MV and RESON systems, respectively. We assume a digitizing error of $<$10 m when extracting cross sections and include a 1-σ error associated with the mean dL/dt of 1.5 m d^{-1}. Propagation in quadrature of these uncertainty contributions gives an uncertainty of ±1.5 m d^{-1} in our melt rate estimates. We present further support for our assumptions as supporting information.

2.3. Subglacial Hydrology

We constrain the geometry of the near-terminus subglacial hydrologic system using two lines of evidence. First, we identify sediment plumes emerging at the terminus of the glacier from 63 Landsat 7, Landsat 8 (30 m horizontal resolution), and Advanced Spaceborne Thermal Emissivity and Reflection Radiometer (15 m horizontal resolution) images between 2008 and 2013, with an average time interval between images of ~1.5 weeks during the summer. We manually digitize sediment plume boundaries and interpret the glacier

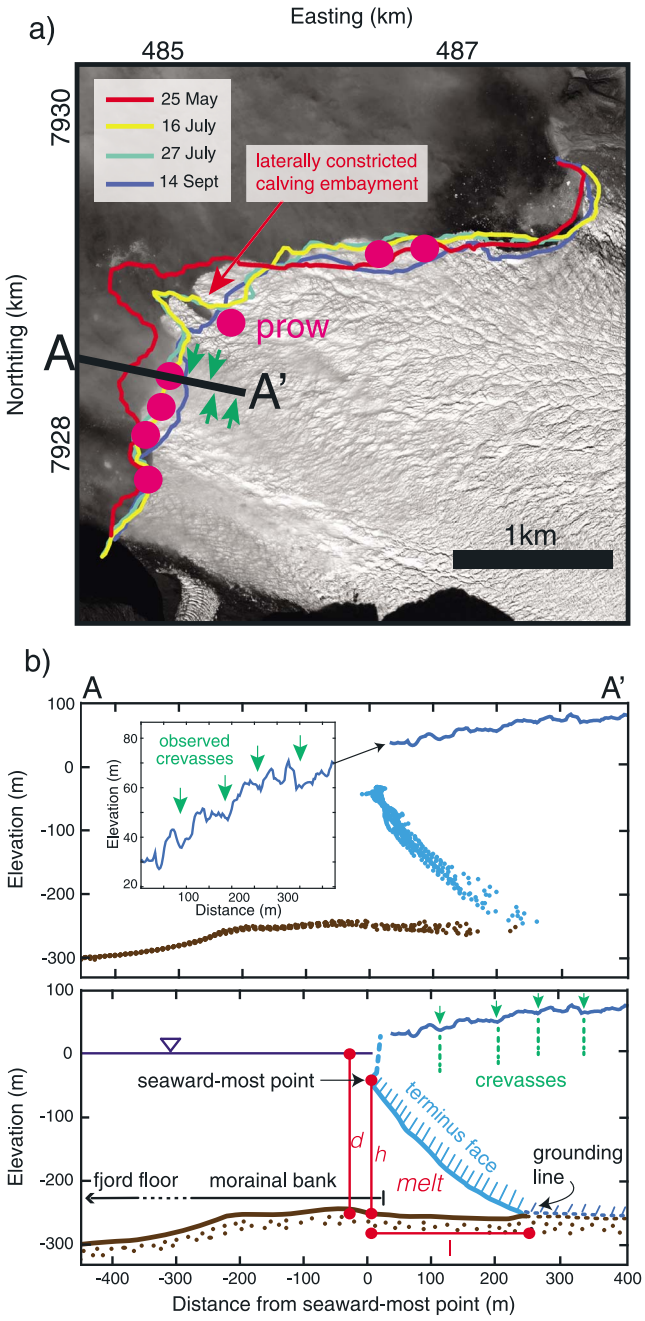


Figure 3. Terminus position and morphology. (a) WorldView-2 imagery (13 July 2012; © DigitalGlobe, 2012) with summer 2013 terminus positions (© DLR, 2013). Pink dots are channel outlets, and green arrows are locations of surface crevasses along transect A-A′. (b) Transect (A-A′) marks the location of the multibeam point cloud. Top panel shows raw multibeam data: bathymetry (brown) and submarine calving face (light blue). Glacier surface (dark blue) is from 2 m resolution SETSM DEM, derived from the image in Figure 3a. Inset shows vertically exaggerated glacier surface and crevasse locations. Bottom panel shows labeled schematic of top panel.

terminus/sediment plume interface as the location where subglacial meltwater actively outflows from a subglacial channel (Figure 4b).

Second, we determine the likely locations of subglacial channels by calculating the gradient in the hydraulic potential (Φ) [*Shreve*, 1972];

$$\nabla\Phi = \nabla(\rho_i g(Z_s - Z_b) + \rho_w g Z_b)$$

where ρ_i and ρ_w are the densities of ice and fresh water, Z_s and Z_b are the ice surface [*Howat et al.*, 2014] and bed elevation [*Morlighem et al.*, 2014], and g is the acceleration due to gravity. We present uncertainty in the location of modeled subglacial flowpaths by adding white noise scaled to the reported uncertainty of the input data sets at each grid point and recalculate the hydraulic potential gradient for 100 calculations (Figures 1 and 4b).

2.4. Surface Crevasses

In order to evaluate the ability of terminus undercutting to vertically connect with surface crevasses, we compare the spacing of adjacent surface crevasses to the length of undercutting beneath them. Surface crevasses near the KS terminus are identified along a longitudinal profile striking up-glacier using a WorldView-2 satellite image (0.5 m horizontal resolution) from 13 July 2012 (A-A′ in Figure 3). We measure distances between observed crevasses near the terminus and quantify their mean spacing (Figure 3b). We then sample the ice surface elevation along the longitudinal profile to get the elevation of observed crevasses using a Surface Extraction from TIN-Based Search Minimization digital elevation model (SETSM DEM) tile derived from the same WorldView-2 image [*Noh and Howat*, 2015] (Figure 3a).

3. Results

KS terminates in water up to 275 m deep atop a broad morainal bank; the glacier fjord is 5 km wide at the ice front (Figures 1 and 2). At the center of the KS terminus is a region, which we term the "prow," which extends into the fjord and divides the terminus into northern and southern portions (Figure 1). Satellite imagery reveals the seasonal evolution of the glacier terminus; between

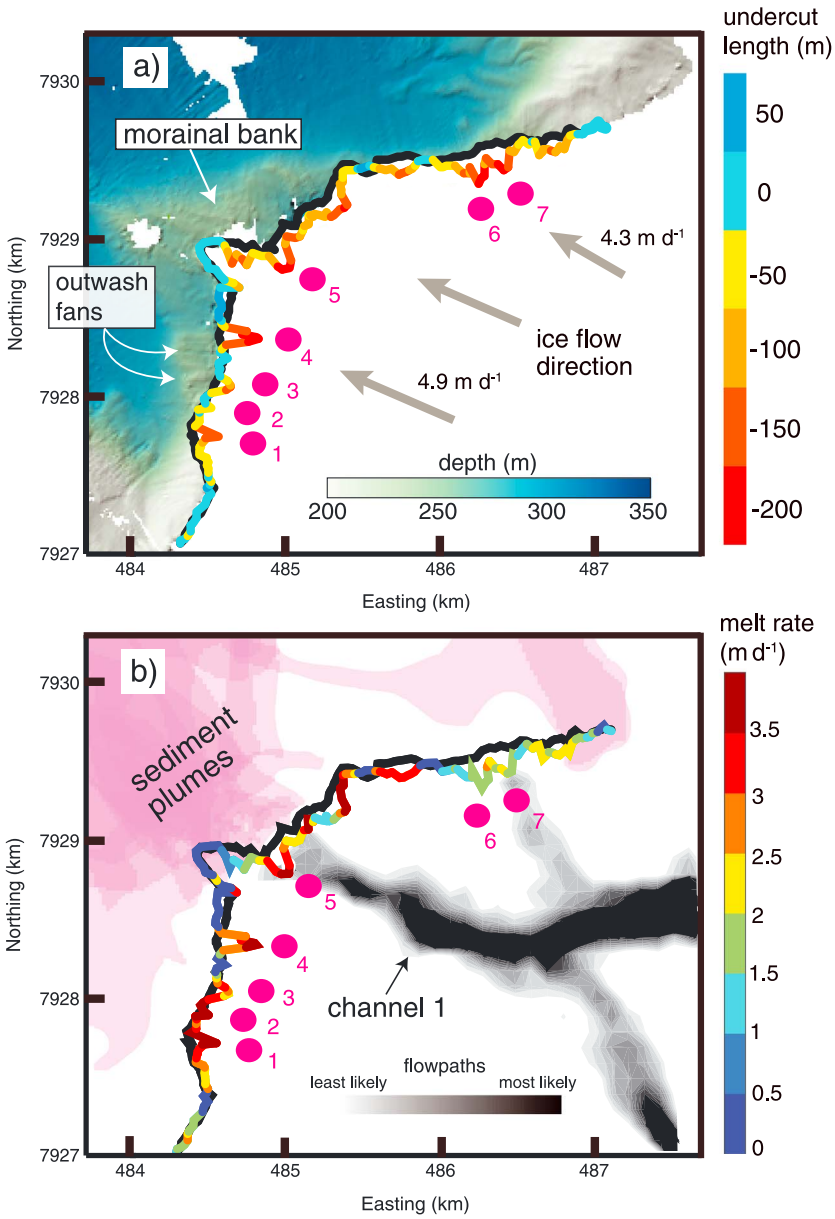


Figure 4. Terminus undercutting and submarine melt rates. Map view of KS near-terminus region and proglacial bathymetry. Pink dots show locations of subglacial discharge outlets. Black line at terminus represents top-most (closest to tidewater line, approximating glacier terminus) multibeam returns. Colored line marks the position of the grounding line constrained from multibeam data (refer to Figure 3b) with color scale representing (a) the terminus undercut length and (b) the estimated submarine melt rate for each terminus-normal cross section. Morainal bank and associated outwash fan deposits are shown for reference. Observed sediment plumes (2008–2013) are shown as pink overlays. Modeled subglacial water flowpaths are shown in gray scale.

May and September 2013, the largest terminus retreat (~500 m) occurred at the prow, with <50 m retreat elsewhere (Figure 3a).

The subglacial hydraulic potential reveals two well-defined subglacial channel flowpaths within 10 km of the KS terminus that sit beneath surface elevation troughs ~70 m lower than their adjacent across flow high points (Figures 1 and 4b). Closer to the terminus, the majority of meltwater coalesces into a single subglacial channel (channel 1 in Figures 1 and 4b) that discharges at the terminus prow (Figure 1). A second channel (channel 2) may—within the hydropotential uncertainty—discharge across the northern terminus face (Figures 1 and 4b). Along the southern terminus face the hydropotential results suggest that meltwater is

drawn from a small region close to the terminus that is not part of the main upstream-channelized system; i.e., no large subglacial discharge flow paths are mapped in this vicinity (Figures 1 and 4b).

Sediment plumes identified in satellite imagery at the fjord surface are consistent with the geometry of the modeled near-terminus subglacial hydraulic gradient and associated subglacial flowpaths. Approximately 95% of sediment plumes observed between 2008 and 2013 occur at the terminus prow (Figure 4b). The persistent occurrence of sediment plumes at the terminus prow verifies that the large subglacial channel discharging there is a stable feature within the subglacial hydraulic gradient over multiple years. The remaining sediment plumes occur along the northern portion of the terminus, adjacent to smaller, secondary channels identified within the hydropotential uncertainty (Figure 4b). We do not observe plumes along the southern terminus face, where we also do not expect major subglacial discharge flow paths.

Side-looking multibeam bathymetry reveals lateral and vertical heterogeneity in the submarine terminus face morphology (Figures 2, 3b, 4a, and S2 in the supporting information). We find that roughly 80% of the submarine terminus face is undercut with a mean undercut length across the entire terminus of 45 m (Figure 4a). Buoyancy forces do not increase either h or l because the terminus is well grounded, with the ice surface elevation >10 m above flotation almost everywhere within the terminus region (Figure S1). The largest undercut feature in our survey is found at the terminus prow (h~150 m and 220 m wide) (outlet #5 in Figures 2, 4, and S3 and Movie S2 in the supporting information). This laterally constricted submarine tunnel has an arched roof rising to within 50 m of sea level and a back that was not imaged by our multibeam system ($l > 200$ m). It coincides with the outlet of the predicted subglacial channel at the terminus prow (channel #1) and the most common location for sediment plume formation (Figure 4b). Based on this evidence, we interpret the observed submarine tunnel mouth as the discharge outlet for the main subglacial channel (channel #1).

The multibeam bathymetry also reveals significant terminus face complexity outside of the main discharge outlet at the terminus prow. We identify six vaulted and laterally constricted submarine cavities in the terminus face (outlets #1–4 and #6 and 7) that are smaller than the tunnel mouth (with l and h both greater than 150 m; Figures 2 and 4a). These cavities are unassociated with sediment plumes observed at the fjord surface. While the outlet at the main subglacial channel appears as an open tunnel within the terminus face, these cavities share a relatively smooth, sloping cavity roof that dips up-glacier (Figure 3b). The angle between a vertical line and the cavity roofs within these large cavities is consistently between 40 and 47° (Figure 3b). Based on their unique morphology, that is, severely undercut with sloping cavity roofs over a narrow width of the terminus (~50 m), we interpret these features as additional outlets for concentrated subglacial discharge, which we term secondary discharge outlets. Outside of these outlets, the submarine terminus face is more gently and moderately undercut or, in rare cases, overcut (Figures 4a and S2c).

We find four large discharge outlets along the southern terminus face (outlets #1–4 in Figure 4 and Movie S3) that appear outside of the modeled subglacial channel system. Here the outlets are spaced approximately 200 m apart and the largest cavity, outlet #4, is similar in size to the tunnel mouth at the terminus prow (h~150 m, l~220 m, and ~150 m wide; Figure 2 and Movie S1). We also see evidence in the multibeam bathymetry for two zones of deltaic sediment deposition (outwash fans) from subglacial discharge, which rise up to 30 m above the morainal bank immediately seaward of discharge outlets #3 and #4 (Figure 4a). This deposition occurs despite no evidence of sediment plumes at the fjord surface or subglacial channels in the hydropotential gradient there. The outwash fan deposits have sediment volumes of $\sim 7.2 \times 10^5$ m^3 and 5.0×10^5 m^3 above the surrounding morainal bank crest, respectively, representing the sediment load deposited from the adjacent discharge outlets. Our observations suggest that these outlets draw water from a small subglacial catchment close to the terminus.

Computed depth-averaged melt rate estimates are heterogeneous across the terminus with the largest melt rates located at the seven submarine discharge outlets, ranging from 2.3 to 3.7 m d^{-1} (Figure 4b). These seven discharge outlets account for 45% of the total submarine melt across the glacier terminus with an average of 1.6 m d^{-1} melt outside of the discharge outlets. The main subglacial channel outlet at the terminus prow (outlet #5) drives approximately 12% of the total estimated submarine melt across the terminus. This indicates that when combined, secondary discharge outlets drive the majority of melt despite drawing discharge from outside the main subglacial channel system (Figure 4b). As a result, the observed discharge outlet configuration disperses melt across the terminus face rather than focusing melt at one centralized

location near the terminus prow [cf. *Xu et al.*, 2013]. Across the entire terminus, the melt rate averages 2.0 m d^{-1}; the total flux of ice lost due to submarine melt is 0.0018 ± 0.0011 km^3 d^{-1}, $36 \pm 20\%$ of the total, full-thickness ice flux delivered to the KS terminus.

WorldView-2 satellite images show that the near-terminus glacier surface is heavily crevassed. The mean distance between adjacent surface crevasses is 80 m directly above discharge outlet #4, a spacing that enables at least two crevasses above the section of the terminus undercut there by ~200 m (Figure 3). Satellite imagery confirms that the distance between adjacent surface crevasses here is representative of crevasse spacing across the entire terminus.

4. Discussion

While the magnitude of the calculated submarine melt rate at KS is similar to that determined elsewhere for similarly sized Greenlandic tidewater glaciers [*Rignot et al.*, 2010], we find heretofore unidentified heterogeneity in melt rates, largely driven by the presence of seven identified discharge outlets distributed across the terminus. While the largest discharge outlet at the terminus prow is associated with predicted subglacial flowpaths, persistent sediment plumes, and anticipated large submarine melt [*Xu et al.*, 2013; *Kimura et al.*, 2014], we also demonstrate that the near-terminus, distributed hydrologic system drives significant submarine melt through minor discharge outlets elsewhere. We observe melt rates exceeding 3.0 m d^{-1} at smaller, secondary discharge outlets outside of the main subglacial channel system, particularly along the southern terminus face. We expect relatively small subglacial discharge fluxes here compared to the main subglacial channel since these locations are unassociated with sediment plumes or predicted subglacial discharge flow paths. The lack of sediment plumes observed at the fjord surface does not necessarily discount subglacial discharge entirely. However, fluxes from these outlets must be small or they would appear at the surface of the shallow, 275 m deep KS fjord [*Carroll et al.*, 2015]. Our observations highlight the importance of considering smaller discharge outlets within a more distributed system when modeling terminus-averaged submarine melt rates.

Our results show the morphological complexity of the submarine terminus and provide observational support for long-standing assumptions of terminus undercutting due to submarine melt [*Motyka et al.*, 2003]. We find significant undercutting across the terminus face, due in large part to distributed subglacial discharge through secondary discharge outlets. This complexity has several important consequences. First, undercutting of the terminus face through melting can trigger calving [*O'Leary and Christoffersen*, 2013; *Bartholomaus et al.*, 2013; *Chauché et al.*, 2014]. The dominant mode of calving at KS is through serac failure, likely by mechanical failure of the ice column from upward melting of undercut cavity roofs eventually connecting to finely spaced surface crevasses (Figure 3b). Indeed, we see in both field observations and satellite imagery that the along-flow width of icebergs calving near the heads of discharge outlets along the southern terminus face often matches the spacing between adjacent surface crevasses there (~80 m), most likely isolated by undercutting following extensional crevassing. We also find greater rates of calving at the subglacial channel near the terminus prow, where melting is largest. Here satellite images often show the formation of a laterally constricted calving embayment at the location of the subglacial channel outlet below (Figures 1 and 3a). Similar crenulated terminus geometries have been linked to submarine melt from channelized runoff at other tidewater glaciers [*Sikonia and Post*, 1980; *Bartholomaus et al.*, 2013; *Chauché et al.*, 2014].

Existing models of submarine melt and near-terminus water circulation assume vertical, planar tidewater glacier termini [*Jenkins*, 2011; *Xu et al.*, 2012, 2013; *Sciascia et al.*, 2013; *Carroll et al.*, 2015; *Slater et al.*, 2015]. Our observations emphasize the need to account for the full 3-D context at the ice/ocean interface when considering buoyant outflow plume dynamics. We expect that buoyant outflow plumes are constricted both by the overhanging roof and the lateral walls within the observed discharge outlets. A small discharge flux released at an undercut, sloping (~45°) interface might produce a plume that has more time to entrain ambient water, thus achieving neutral buoyancy at a lower depth than if the terminus were vertical. Such feedback would explain how relatively small discharge fluxes from secondary outlets can drive melt rates nearly as high as are found at the main subglacial channel. Current models suggest undercutting could reduce plume entrainment by forcing nonvertical upwelling [*Jenkins*, 2011], or by restricting plume/fjord water contact. We argue that the discrepancy between these models and our results must be rectified.

5. Conclusion

Discharge-driven submarine melt provides a dynamic coupling between glacier and ocean systems. Our results present much-needed constraints on the geometry of subglacial discharge outlets, the shape of the submarine terminus face, and the impact that these variables have on the spatial distribution of melt across the terminus. We find that distributed discharge outside of dominant channels can induce significant melt at locations not identified using hydraulic potential analyses alone [e.g., *Rignot et al.*, 2015]. While concentrated subglacial discharge can play an essential role in fjord circulation [*Motyka et al.*, 2013; *Carroll et al.*, 2015; *Straneo and Cenedese*, 2015], subglacial water dispersed over the width of the submarine terminus through smaller discharge outlets can also control the rate and distribution of submarine melt. The combination of ice/ocean interface observations with ice surface and bed elevation data sets has revealed new insights into the geometric and mechanical relationship between undercutting and calving. We suggest that terminus undercutting can destabilize the ice front by connecting to surface crevasses. To better represent the ice-ocean boundary in prognostic models of the Greenland Ice Sheet, numerical models may need to account for the three-dimensional complexity of the submarine terminus face and assess the importance of rapid melt at more abundant, small-discharge outlets.

Acknowledgments
This work was completed at the University of Texas at Austin and funded by NASA grant NNX12AP50G and a seed grant from the Jackson School of Geosciences, University of Texas at Austin. We thank Christian Black and David Jonathan Peters for their assistance in digitizing sediment plumes and terminus positions. We thank Alun Hubbard, an anonymous reviewer, and the Editor for their helpful comments that greatly improved the manuscript.

References

Bartholomaus, T. C., C. Larsen, and S. O'Neel (2013), Does calving matter? Evidence for significant submarine melt, *Earth Planet. Sci. Lett.*, *380*, 21–30.
Carroll, D., D. A. Sutherland, E. L. Shroyer, J. D. Nash, G. Catania, and L. A. Stearns (2015), Modeling turbulent subglacial meltwater plumes: Implications for fjord-scale buoyancy-driven circulation, *J. Phys. Oceanogr.*, *45*, 2169–2185.
Chauché, N., A. Hubbard, J.-C. Gascard, J. E. Box, R. Bates, M. Koppes, A. Sole, P. Christoffersen, and H. Patton (2014), Ice–ocean interaction and calving front morphology at two west Greenland tidewater outlet glaciers, *Cryosphere*, *8*, 1457–1468.
Cuffey, K., and W. Paterson (2010), *The Physics of Glaciers*, 4th ed., 704 p., Butterworth-Heinemann, Burlington, Mass.
Enderlin, E. M., I. M. Howat, S. Jeong, M. J. Noh, J. H. Angelen, and M. R. Broeke (2014), An improved mass budget for the Greenland ice sheet, *Geophys. Res. Lett.*, *41*, 866–872, doi:10.1002/2013GL059010.
Ettema, J., M. R. van den Broeke, E. van Meijgaard, W. J. van de Berg, J. L. Bamber, J. E. Box, and R. C. Bales (2009), Higher surface mass balance of the Greenland Ice Sheet revealed by high-resolution climate modeling, *J. Geophys. Res.*, *36*, L12501, doi:10.1029/2009GL038110.
Howat, I. M., A. Negrete, and B. E. Smith (2014), The Greenland Ice Mapping Project (GIMP) land classification and surface elevation datasets, *Cryosphere*, *8*, 453–478.
Inall, M. E., T. Murray, F. R. Cottier, K. Scharrer, T. J. Boyd, K. J. Heywood, and S. L. Bevan (2014), Oceanic heat delivery via kangerdlugssuaq fjord to the south-east greenland ice sheet, *J. Geophys. Res. Oceans*, *119*, 631–645, doi:10.1002/2013JC009295.
Jenkins, A. (2011), Convection-driven melting near the grounding lines of ice shelves and tidewater glaciers, *J. Phys. Oceanogr.*, *41*, 2279–2294.
Joughin, I., B. Smith, I. Howat, and T. Scambos (2014), *MEaSUREs Greenland Ice Velocity: Selected Glacier Site Velocity Maps from InSAR*, NASA Natl. Snow and Ice Data Center Distrib. Active Arch. Center, Boulder, Colo.
Kimura, S., P. R. Holland, A. Jenkins, and M. Piggot (2014), The effect of meltwater plumes on the melting of a vertical glacier face, *J. Phys. Oceanogr.*, *44*, 3099–3117.
Morlighem, M., E. Rignot, J. Mouginot, H. Seroussi, and E. Larour (2014), Deeply incised submarine glacial valleys beneath the Greenland Ice Sheet, *Nat. Geosci.*, *7*, 418–422.
Motyka, R., L. Hunter, K. Echelmeyer, and C. Connor (2003), Submarine melting at the terminus of a temperate tidewater glacier, LeConte Glacier, Alaska, USA, *Ann. Glaciol.*, *36*, 57–65.
Motyka, R., et al. (2011), Submarine melting of the 1985 Jakobshavn Isbrae floating ice tongue and the triggering of the current retreat, *J. Geophys. Res.*, *116*, F01007, doi:10.1029/2009JF001632.
Motyka, R., W. P. Dryer, J. Amundson, M. Truffer, and M. Fahnestock (2013), Rapid submarine melting driven by subglacial driven by subglacial discharge, LeConte Glacier, Alaska, *Geophys. Res. Lett.*, *40*, 1–6, doi:10.1002/grl.51011.
Murray, T., et al. (2010), Ocean regulation hypothesis for glacier dynamics in southeast Greenland and implications for ice sheet mass changes, *J. Geophys. Res.*, *115*, F03026, doi:10.1029/2009JF001522.
Nick, F. M., A. Vieli, I. M. Howat, and I. Joughin (2009), Large-scale changes in Greenland outlet glacier dynamics triggered at the terminus, *Nat. Geosci.*, *2*, 110–114.
Noh, M. J., and I. M. Howat (2015), Automated stereo-photogrammetric DEM generation at high latitudes: Surface Extraction from TIN-Based Search Minimization (SETSM) validation and demonstration over glaciated regions, *GIScience Remote Sens.*, *52*, 198–217.
O'Leary, M., and P. Christoffersen (2013), Calving on tidewater glaciers amplified by submarine frontal melting, *Cryosphere*, *7*, 119–128.
Rignot, E., M. Koppes, and I. Velicogna (2010), Rapid submarine melting of the calving faces of west greenland glaciers, *Nat. Geosci.*, *3*, 187–191.
Rignot, E., I. Velicogna, M. R. van den Broeke, A. Monaghan, and J. Lenaerts (2011), Acceleration of the contribution of the Greenland and Antarctic ice sheets to sea level rise, *Geophys. Res. Lett.*, *38*, L05503, doi:10.1029/2011GL047109.
Rignot, E., I. Fenty, Y. Xu, C. Cai, and C. Kemp (2015), Undercutting of marine-terminating glaciers in West Greenland, *Geophys. Res. Lett.*, *42*, 5909–5917, doi:10.1002/2015GL064236.
Sciascia, R., F. Straneo, C. Cenedese, and P. Heimbach (2013), Seasonal variability of submarine melt rate and circulation in an East Greenland fjord, *J. Geophys. Res. Oceans*, *118*, 2492–2506, doi:10.1002/jgrc.20142.
Seale, A., P. Christoffersen, R. I. Mugford, and M. O'Leary (2011), Ocean forcing of the Greenland Ice Sheet: Calving fronts and patterns of retreat identified by automatic satellite monitoring of eastern outlet glaciers, *J. Geophys. Res.*, *116*, F03013, doi:10.1029/2010JF001847.
Shepherd, A., et al. (2012), A reconciled estimate of ice-sheet mass balance, *Science*, *338*, 1183–1189.
Shreve, R. L. (1972), Movement of water in glaciers, *J. Glaciol.*, *11*(62), 205–214.

Sikonia, W. G., and A. Post (1980), Columbia Glacier, Alaska: Recent ice loss and its relationship to seasonal terminal embayments, thinning, and glacial flow, *U.S. Geol. Surv. Hydrol. Invest. Atlas*, *619*, 1–3.

Slater, D. A., P. W. Nienow, T. R. Cowton, D. N. Goldberg, and A. J. Sole (2015), Effect of near-terminus subglacial hydrology on tidewater glacier submarine melt rates, *Geophys. Res. Lett.*, *42*, 2861–2868, doi:10.1002/2014GL062494.

Straneo, F., and C. Cenedese (2015), The dynamics of Greenland's glacial fjords and their role in climate, *Annu. Rev. Mar. Sci.*, *7*, 89–112.

Straneo, F., et al. (2011), Impact of fjord dynamics and glacial runoff on the circulation near Helheim Glacier, *Nat. Geosci.*, *4*, 322–327.

van den Broeke, M. R., J. Bamber, J. Ettema, E. Rignot, E. Schrama, W. J. van de Berg, E. van Meijgaard, I. Velicogna, and B. Wouters (2009), Partitioning recent Greenland mass loss, *Science*, *326*, 984–986.

Xu, Y., E. Rignot, D. Menemenlis, and M. Koppes (2012), Numerical experiments on subaqueous melting of Greenland tidewater glaciers in response to ocean warming and enhanced subglacial discharge, *Ann. Glaciol.*, *53*(60), 229–234.

Xu, Y., E. Rignot, D. Menemenlis, and M. Mar Flexas (2013), Subaqueous melting of Store Glacier, west Greenland from three-dimensional, high-resolution numerical modeling and ocean observations, *Geophys. Res. Lett.*, *40*, 4648–4653, doi:10.1002/grl.50825.

Geophysical Research Letters

Supporting Information for

Distributed subglacial discharge drives significant submarine melt at a Greenland tidewater glacier

M. J. Fried,[1,2*] G. A. Catania,[1,2] T. C. Bartholomaus,[1] D. Duncan,[1] M. Davis,[1]
L. A. Stearns,[3] J. Nash,[4] E. Shroyer[4] & D. Sutherland[5]

[1]Institute for Geophysics, University of Texas, Austin TX, 78759
[2]Department of Geology, University of Texas, Austin TX, 78713
[3]Department of Geology, University of Kansas, Lawrence, KS, 66045
[4]College of Earth, Ocean & Atmos. Sciences, Oregon State University, Corvalis OR, 97331
[5]Department of Geological Sciences, University of Oregon, Eugene, OR, 97403
[*]Corresponding author: mfried@ig.utexas.edu

Contents of this file

1. Text S1: Other sources of undercutting
2. Figure S1: Height above flotation map
3. Figure S2: Submarine terminus face morphologies
4. Figure S3: Terminus prow discharge outlet

Additional Supporting Information (Files uploaded separately)

5. Movie S1: Discharge outlet #4 morphology
6. Movie S2: Discharge outlet #5 morphology
7. Movie S3: Southern terminus face morphology and bathymetry
8. Movie S4: Pan of submarine terminus

Introduction

The figures and movies included in this supplement provide additional information and context supporting the conclusion of the main text. The supplementary visuals use multibeam bathymetry data in order to highlight the complex morphology of the submarine glacier terminus face and the numerous undercut discharge outlets of varying sizes across the terminus.

Text S1

We assess other potential contributors to undercutting at the glacier front by evaluating the likelihood of upward flexure at the terminus due to buoyancy forces and estimating the size of subglacial channels. We find that the KS terminus is above flotation using several lines of evidence. First, we produce a height above flotation map (Fig. S1) using GIMP ice surface (Howat et al., 2014) and mass conserving bed elevation (Morlighem et al. 2014) datasets in the equation for hydrostatic equilibrium. The map reveals that the entire terminus region is 10 m - 200 m above flotation. Second, we do not find surface relaxing or closing of surface crevasses in longitudinal profiles near the terminus (in available World-View images) that would accompany upward flexure.

We use a model of subglacial channel cross-sectional area (Schoof, 2010) to estimate the upper limit of conduit enlargement at the terminus. We assume that channels there are on the order of 20 m wide, flow at capacity along the hydraulic gradient and experience no creep closure due to water pressure at overburden. Under these conditions, modeled channels widen radially at ~1 m d^{-1}. Integrated over the observation period coincident with our measurements of terminus position change, this yields a 20 m conduit radius and accounts for 11% of the observed outlet size at the terminus prow. At secondary discharge outlets, particularly along the southern terminus face, conduit sizes and their discharge are likely smaller, diminishing the potential contribution of conduit enlargement by viscous energy dissipation.

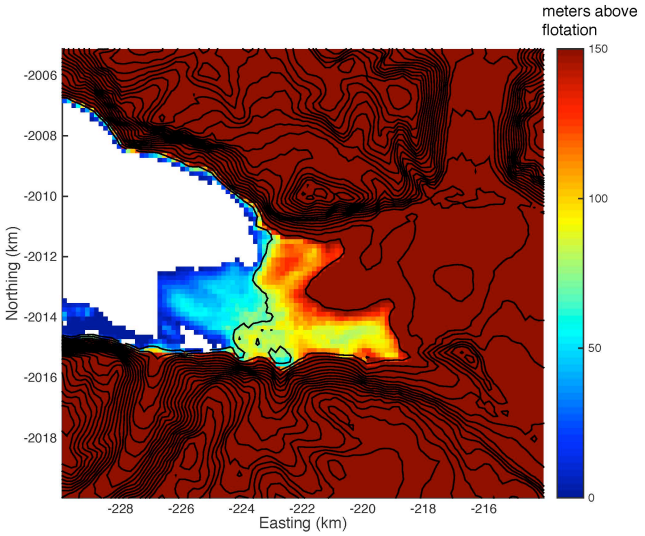


Figure S1. Height above flotation map for KS terminus region. Colorscale is meters above flotation.

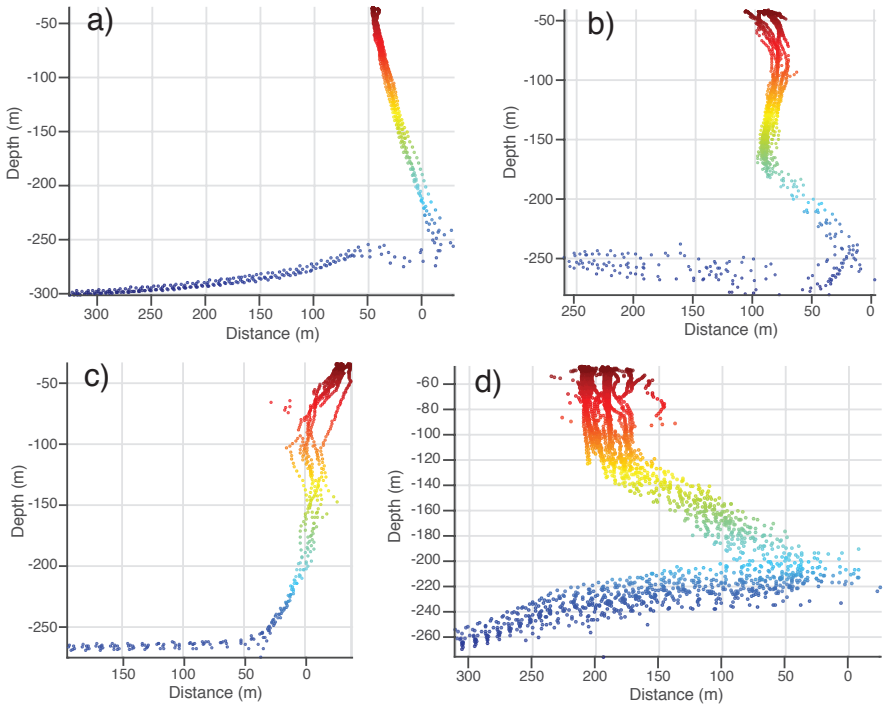


Figure S2. Cross-sections through multibeam data showing the range of submarine terminus face morphologies. Scales for x- and y-axes on each panel are identical. a) gently undercut terminus face not co-located with a channel outlet, showing the top of the morainal bank at 50 m. b) undulating terminus face. c) overcut terminus face. d) discharge outlet #6.

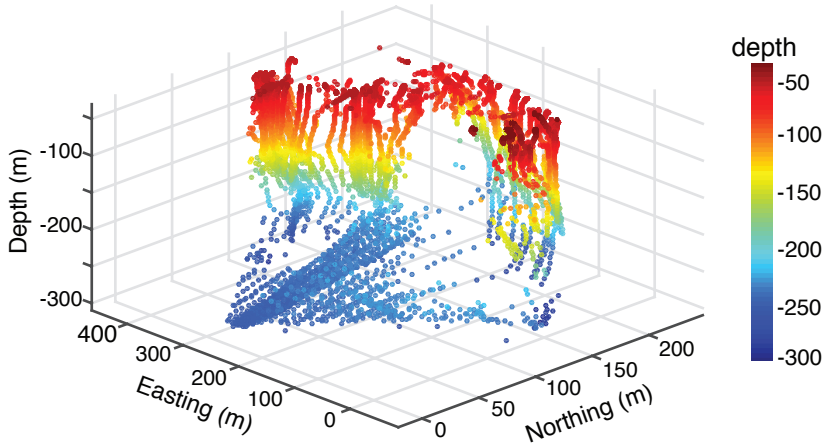


Figure S3. Oblique-view through multibeam data showing the terminus prow discharge outlet (discharge outlet #5).

Files uploaded separately

Movie S1. Discharge outlet #4 morphology. View of the submarine terminus face morphology around discharge outlet #4. Movie starts looking normal to terminus face front and then pivots counter-clockwise around the terminus backside to illustrate undercutting.

Movie S2. Discharge outlet #5 morphology. View of the tunnel mouth morphology around discharge outlet #5 at the terminus prow. Movie starts looking normal to terminus face front and then pivots counter-clockwise.

Movie S3. Southern terminus face morphology and bathymetry. View of the submarine terminus face morphology and bathymetry south of the terminus prow. Movie starts looking normal to terminus face front and then pivots counter-clockwise around the terminus backside to illustrate isolated undercutting around discharge outlets.

Movie S4. Pan of the submarine terminus. Movie starts on the northern margin and pans south across the terminus face.

References:

Schoof, C. (2010), Ice-sheet acceleration driven by melt supply variability, *Nature*, *468* (7325), 803-806, doi:10.1038/nature09618.